Simulation of Fragmentation with Material Point Method Based on Gurson Model and Random Failure

Pengfei Yang[1], Yan Liu[1], Xiong Zhang[1, 2], Xu Zhou[3] and Yuli Zhao[3]

Abstract: The material point method is extended to the simulations of fragmentation driven by detonation. A crack modeling scheme based on contact algorithm with material failure process is developed to study the dynamic crack propagation in plastic media. When considering microscopic damage of material, the plastic behavior is described by Gurson model with randomly-distributed initial void of material points. Gurson model can degenerate to J_2 plastic theory while the microscopic void is ignored, in which situation the Weibull random failure scheme will be used. Meanwhile, a background-grid-based searching method is proposed to capture the statistical feature of the fragmentation. The scaling of the fragments in simulation tends to exhibit the same law as that in the experiment. It is found that the material point method possesses great potential for simulating high strain-rate, large deformation fragmentation phenomena.

Keywords: material point method, fragmentation, Gurson model, Weibull random, material failure

1   Introduction

Sequential fracture leads to fragmentation. One of the most important aspects of dynamic fracture is that the body, at the end of fracturing sequence, is divided into many parts [Meyers (1994)]. Fragmentation driven by detonation is a highly complex phenomenon which involves high-rate strain and multi-phase material interaction. The fragmenting material expands after detonation and break up abruptly, producing high speed fragments of different shapes and sizes. Driving the material with high explosives has been commonly employed to investigate the phenomenon of high-rate fracture and fragmentation [Goto, Becker, Orzechowski, Springer, Sunwoo and Syn (2008); Arnold, Rottenkolber (2008)].

---

[1] School of Aerospace, Tsinghua University, Beijing 100084, China.

[2] Corresponding author: xzhang@tsinghua.edu.cn

[3] Beijing Institute of Special Engineering Design and Research, Beijing 100028, China.

The random characterization of the fragmentation can be described by both microscopic defect and macroscopic failure. The material microscopic defect can be represented by Gurson model [Gurson (1977)] in which the initial void fraction is randomly distributed, and the macroscopic failure value can be specified by the Weibull form [Weibull (1939, 1951)]. Ductile fracture of metals usually occurs within plastic deformation through the nucleation, growth and coalescence of small voids. This mechanism is operative under high strain rate conditions in problems involving impact [Gurran, Seaman and Shockey (1987)] and explosive forming [Worswick, Pick (1990)]. When analyzing unstable cleavage fracture, the Weibull theory is normally used [Beremin (1983); Wang (1991)]. As it is known, the ductile fracture happens at low loading rates (or high temperatures) and brittle fracture at high loading rates(or low temperatures). Under typical conditions, a crack initiates and grows through ductile tearing and ultimately fails due to catastrophic cleavage fracture. The competition of ductile tearing and cleavage fracture controls the ductile/brittle transition [Lin, Shin (1996)].

Behavior of explosion is complicated and usually involves extreme large deformation and multi-material interaction of different phases [Zukas, Walters (1998)], which gives rise to difficulties and challenges for traditional numerical methods. The Lagrangian finite element method (FEM) suffered from mesh distortion and element entanglement. Moreover, a non-physical element erosion algorithm is often incorporated. Eulerian methods are capable of handling extreme large deformation, but efforts must be taken to treat material interfaces and free surfaces. Recently-developed particle methods, such as Smoothed Particle Hydrodynamics (SPH) [Johnson, Stryk and Beissel (1996); Liu, Liu (2003)] and Material Point Method (MPM) [Sulsky, Chen, Schreyer (1994); Sulsky, Zhou, Schreyer (1995)], show many advantages over mesh-based method for problems associated with extremely large deformation. A comparison study of MPM and SPH in modeling hypervelocity impact problems was conducted in [Ma, Zhang, Qiu (2009)].

The Material Point Method (MPM) developed by Sulsky et al. [Sulsky, Chen, Schreyer (1994); Sulsky, Zhou, Schreyer (1995)] is an extension of the FLIP particle-in-cell method [Brackbill, Kothe, Ruppel (1988)] in computational fluid dynamics to the computational solid mechanics. In MPM, the material domain is discretized using a collection of material points, whose movement represents the deformation of the material, thus MPM avoids the difficulty in interface treatment in Eulerian methods. The momentum equations are solved on a predefined regular background grid, so that the grid distortion and entanglement are completely avoided. MPM has been successfully applied to solve many engineering problems, such as film delamination [Shen, Chen (2005)], explosive process [Hu, Chen (2006); Guilkey, Harman, Banerjee (2007)], dynamic fracture [Nairn (2003); Guo, Nairn (2006)],

dynamic analysis of saturated porous media [Zhang, Wang, Chen (2009)], just to name a few.

Numerical approaches to predict crack growth can be based on either knowing values of a crack tip characterizing parameter or incorporating a model of the failure process into the constitutive description of the continuum [Needleman, Tvergaard (2000)]. In this paper, the second approach is used, thus fracture emerges as a natural outcome of the deformation history of material points. MPM has advantages over FEM for modeling of crack propagation because the crack is not constrained by grid lines and is free to be oriented and to propagate in any direction. MPM has previously been extended as CRAMP [Nairn (2003); Guo, Nairn (2006)] by introducing multiple nodal velocity fields to analyze explicit cracks and dynamic fracture. The cracks were explicitly described by adding additional massless particles to the standard MPM data structures. Cracks are represented in 2D as a series of line segments [Nairn (2003)], and represented in 3D as a set of triangular elements [Guo, Nairn (2006)]. The determination of velocity fields was the most time-consuming additional calculation in CRAMP, especially for three-dimensional problems [Guo, Nairn (2006)]. Furthermore, the specimens analyzed by CRAMP processed an initially embedded crack, and the deformation of material was relatively small which ensured the determination of velocity fields near the crack surface not too complicated. The metal shell driven by detonation will experience very large deformation, in which situation the influence of the plastic strain should be carefully considered.

In this paper, the material point method is extended to the simulations of fragmentation driven by detonation. To account for the microscopic process of plastic deformation, the Gurson model is implemented in the framework of MPM. A contact method is presented with failure criteria to model the dynamic crack propagation. The material points which lose their capacity of sustaining load are converted to a failed body, which naturally form the crack surfaces. Cracks move under the contact mechanism between the failed and unfailed bodies, thus interpenetrations between crack surfaces are automatically prevented. The methodology can be easily extended so that it can handle arbitrary cracks in three dimensions. Furthermore, it eliminates the need for a surface model of the crack, turning out to be simple and efficient even the material undergoes extreme deformation.

In conventional method, the fragment size was obtained by determining if any two particles belonged to the same cluster. The distance of any two particles must be computed to compare with an arbitrary cutoff distance [Diehl, Carmona, Araripe, Andrade and Farias (2000)]. The method is immediate but inefficient. Owing to the intrinsic characters of MPM, a background-grid-based searching technique is developed here to generate the statistics of fragmentation, which is showed in the

examples to be very efficient.

The proposed schemes have been implemented in MPM3D [Ma, Zhang, Lian and Zhou (2009); Ma, Zhang, Huang (2010)], a three dimensional MPM code developed by the authors using C++ programming language. MPM3D has been applied to solve problems involving extreme deformation and complex problems such as explosion [Ma, Zhang, Lian and Zhou (2009)] and penetration [Ma, Zhang, Huang (2010)].

The paper is organized as follows. A brief description of the material point method is provided in section 2. The stress update algorithm is presented with the Gurson model and the equation of state in section 3. In section 4, the crack model is developed based on the material failure criteria and contact method of MPM. A method based on the background grid of MPM is proposed in section 5 to calculate the statistics of fragmentation. Several numerical examples, including shear band analysis, fragmentation of a cylinder shell, and fragmentation of a sphere shell are illustrated in section 6. Concluding remarks are presented in the last section.

2   Material Point Method

Material point method combines the description of Lagrangian particles and Eulerian background mesh, as illustrated in Figure 1. In the solution phase of MPM, particles are rigidly attached to the background grid and they deform with the grid. The momentum equation are solved in the framework of standard finite element method, and then the positions and velocities of particles are updated by mapping back the obtained kinematic solution on the grid nodes. After that, the deformed grid is discarded in the subsequent time step and a new regular grid is used to avoid mesh distortion. Generally speaking, the same fixed regular grid can be used throughout the simulation.
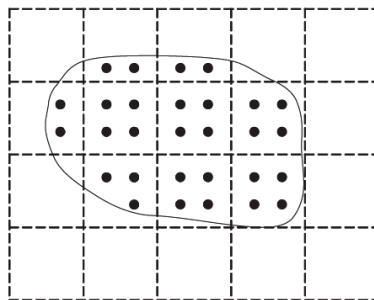

Figure 1: Material point discretization

The momentum equilibrium equation is given as

$$\nabla \cdot \sigma + \rho \mathbf{b} = \rho \mathbf{a} \tag{1}$$

where ρ is the current density, σ is the Cauchy stress, $\mathbf{b}$ is the body force per unit mass, $\mathbf{a}$ is the acceleration.

The weak form of governing equation (1) can be obtained through weighted residual approach as [Sulsky, Chen, Schreyer (1994)]

$$\delta \Pi = \int_\Omega \rho \mathbf{a} \cdot \delta \mathbf{v} d\Omega + \int_\Omega \rho \sigma^s : \nabla \delta \mathbf{v} d\Omega - \int_\Omega \rho \mathbf{b} \cdot \delta \mathbf{v} d\Omega - \int_{\Gamma_t} \rho \bar{\mathbf{t}}^s \cdot \delta \mathbf{v} d\Gamma = 0 \tag{2}$$

where $\sigma^s = \sigma/\rho$ and $\bar{\mathbf{t}}^s = \bar{\mathbf{t}}/\rho$ are the specific stress and specific traction, respectively, $\mathbf{v}$ is the velocity, Γ_t is the boundary portions prescribed with traction.

The material domain Ω is discretized by a collection of material points. Mass, velocity and stress, as well as material parameters and internal variables needed for constitutive models are carried by material points. The density can be approximated as

$$\rho(\mathbf{x}) = \sum_{p=1}^{n_p} m_p \delta(\mathbf{x} - \mathbf{x}_p) \tag{3}$$

where n_p is the total number of material points, m_p is the mass of material point p, δ is Dirac δ, $\mathbf{x}_p$ is the location of material point p. Since the movement of particles represents the deformation of physical domain and mass is carried by particles, the mass conservation is automatically satisfied in MPM.

Because the particles are rigidly attached to the computational grid, a variable $\mathbf{u}$ of particle p can be obtained by mapping from their grid node values $\mathbf{u}_i$ using the standard finite element shape functions of the grid

$$\mathbf{u}_p = \sum_{i=1}^{n_g} N_{ip} \mathbf{u}_i \tag{4}$$

where $N_{ip} = N_i(\mathbf{x}_p)$ is the shape function of grid node i evaluated at the site of particle p. In this paper, 8-point hexahedron element is used as the background grid whose shape function is given by

$$N_{ip} = \frac{1}{8}(1 + \xi_p \xi_i)(1 + \eta_p \eta_i)(1 + \zeta_p \zeta_i); \quad i = 1, 2, \cdots 8 \tag{5}$$

if the particle p (ξ_p, η_p, ζ_p) is located inside the hexahedron, where ξ_i, η_i and ζ_i take ± 1 on gird node i. If the particle p is outside the hexahedron, $N_{ip} = 0$.

Substituting equations (3) and (4) into the weak form equation (2), and invoking the arbitrariness of $\delta\mathbf{v}_i$ yields

$$\dot{\mathbf{p}}_i = \mathbf{f}_i^{\text{int}} + \mathbf{f}_i^{\text{ext}} \tag{6}$$

where

$$\mathbf{p}_i = \sum_{p=1}^{n_p} m_p N_{ip} \mathbf{v}_p \tag{7}$$

is the momentum of node i,

$$\mathbf{f}_i^{\text{int}} = -\sum_{p=1}^{n_p} \nabla N_{ip} \cdot \sigma_p \frac{m_p}{\rho_p} \tag{8}$$

is the internal force, and

$$\mathbf{f}_i^{\text{ext}} = \sum_{p=1}^{n_p} m_p N_{ip} \mathbf{b}_p + \sum_{p=1}^{n_p} N_{ip} h^{-1} \bar{\mathbf{t}}_p^s \frac{m_p}{\rho_p} \tag{9}$$

is the external force.

3 Constitutive modeling

3.1 The Gurson model

The stress tensor of material can be written as

$$\sigma = \sigma_m \mathbf{I} + \frac{2}{3}\sigma_{\text{eq}}\mathbf{n} \tag{10}$$

where $\mathbf{n} = \frac{3}{2\sigma_{\text{eq}}}\mathbf{S}$, $\mathbf{S} = \sigma - \sigma_m\mathbf{I}$ is the deviatoric stress tensor, $\sigma_m = \frac{1}{3}\sigma : \mathbf{I}$ is the mean stress tensor, $\sigma_{\text{eq}} = \left(\frac{3}{2}\mathbf{S} : \mathbf{S}\right)^{1/2}$ is the equivalent stress.
The stress at time $n+1$ is updated by

$$\begin{aligned}
\sigma^{n+1} &= \sigma^{Rn} + \mathbf{C}_s : \mathbf{D}^e \Delta t \\
&= \sigma^{Rn} + \mathbf{C}_s : \left(\mathbf{D} - \mathbf{D}^P\right) \Delta t \\
&= \sigma^{t(n+1)} - \mathbf{C}_s : \mathbf{D}^P \Delta t
\end{aligned} \tag{11}$$

where

$$\sigma^{t(n+1)} = \sigma^{Rn} + \mathbf{C}_s : \mathbf{D}\Delta t \tag{12}$$

is the trial stress, $\mathbf{C}_s$ is the elastic constitutive tensor of the solid, $\mathbf{D}$ is the strain rate tensor, Δt is the time step, $\mathbf{D}^e$ is the elastic strain rate tensor, $\mathbf{D}^p$ is the plastic strain rate tensor, and σ^{Rn} is the stress taking into account the effect of rotation at time n.

The ductile tearing process was simulated using void-containing cell elements by Lin and Shin [Lin, Shin (1996)], in which each cell element contained a centered sphere void of initial fraction. The growth of the void and the associated softening was described by Gurson constitutive relation [Gurson (1977)]. In this paper, each material point is assigned with an initial void volume fraction f_0. The yield condition is given by

$$\Phi = \left(\frac{\sigma_{\text{eq}}}{Y}\right)^2 + 2q_1 f^* \cosh\left(\frac{3q_2\sigma_m}{2Y}\right) - \left(1 + q_1^2 f^{*2}\right) \tag{13}$$

where q_1 and q_2 were introduced by Tvergaard [Tvergaard (1981)] to to bring predictions of the original Gurson model [Gurson (1977)] into closer agreement with full numerical analysis of a periodic array of voids, f^* was introduced by Tvergaard and Needleman [Tvergaard, Needleman (1984)] to account for the rapid void coalescence at failure. In the paper, the Gurson model refers to equation (13) with q_1, q_2 parameters.

$$f^* = \begin{cases} f & \text{for} \quad f \leq f_c \\ f_c + \frac{1/q_1 - f_c}{f_f - f_c}(f - f_c) & \text{for} \quad f_c < f \leq f_f \\ 1/q_1 & \text{for} \quad f > f_f \end{cases} \tag{14}$$

where f is the current void volume fraction, f_c is the critical value of void volume fraction at which void coalescence commences, f_f is the void fraction at which the material is assumed to have lost all load carrying capacity.

In equation (13), Y is the matrix flow stress, which is related to the microscopic, work-equivalent plastic strain $\bar{\varepsilon}^p$ by equating the plastic work of the macroscopic stress with the energy dissipated in plastic deformations at the microlevel by

$$Y = \frac{\sigma : \mathbf{D}^p}{(1-f)\dot{\bar{\varepsilon}}^p} \tag{15}$$

The rate of growth of the void volume fraction accounts for both the expansion of existing void and the nucleation of new voids, namely

$$\dot{f} = \dot{f}_{\text{growth}} + \dot{f}_{\text{nucleation}} \tag{16}$$

where

$$\dot{f}_{\text{growth}} = (1-f)\mathbf{D}^p : \mathbf{I} \tag{17}$$

is the growth rate of existing voids as a function of the plastic volume change.

Void nucleation can be modeled by the strain–controlled formulation proposed by Chu and Needleman [Chu, Needleman (1980)] as

$$\dot{f}_{\text{nucleation}} = A_N(\bar{\varepsilon}^p)\dot{\bar{\varepsilon}}^p \tag{18}$$

where $A_N(\bar{\varepsilon}^p) = \frac{f_N}{s_N\sqrt{2\pi}}\exp\left[-\frac{1}{2}\left(\frac{\bar{\varepsilon}^p - \varepsilon_N}{s_N}\right)^2\right]$, s_N and ε_N are the standard deviation and the mean value of the distribution of the nucleation strain, f_N is the total void volume fraction that can be nucleated.

By assuming the associated flow rule, $\mathbf{D}^p$ can be obtained from the normality rule as

$$\mathbf{D}^p = \lambda\frac{\partial\Phi}{\partial\sigma} = \lambda\left\{\frac{1}{3}\frac{\partial\Phi}{\partial\sigma_m}\mathbf{I} + \frac{\partial\Phi}{\partial\sigma_{\text{eq}}}\mathbf{n}\right\} = \frac{1}{3}D_m^p\mathbf{I} + D_{\text{eq}}^p\mathbf{n} \tag{19}$$

where $D_m^p = \lambda\frac{\partial\Phi}{\partial\sigma_m}$, $D_{\text{eq}}^p = \lambda\frac{\partial\Phi}{\partial\sigma_{\text{eq}}}$ [Simonsen, Li (2004)]. Substituting equation (19) into equation (11) leads to

$$\sigma^{n+1} = \sigma^{*(n+1)} - KD_m^p\mathbf{I}\Delta t - 2GD_{\text{eq}}^p\mathbf{n}\Delta t \tag{20}$$

where $K = (1-f)K_s$ and $G = (1-f)G_s$, K_s and G_s are the bulk modulus and shear modulus of the solid (matrix), given by $K_s\mathbf{I} = \frac{1}{3}\mathbf{C}:\mathbf{I}$ and $2G_s\mathbf{n} = \mathbf{C}:\mathbf{n}$.

The mean stress and the equivalent stress are updated by

$$\sigma_m^{n+1} = \sigma_m^{t(n+1)} - KD_m^p\Delta t \tag{21}$$

$$\sigma_{\text{eq}}^{n+1} = \sigma_{\text{eq}}^{t(n+1)} - 3GD_{\text{eq}}^p\Delta t \tag{22}$$

The deviatoric stress could be calculated by $\mathbf{S}^{n+1} = \mathbf{S}^{t(n+1)}\frac{\sigma_{\text{eq}}^{n+1}}{\sigma_{\text{eq}}^{t(n+1)}}$.

It should be noticed that, in the absence of voids, i.e. $f = 0$, the model reduces to J_2-flow theory of plasticity with isotropic hardening.

3.2 Equation of state (EOS)

The pressure of both the gaseous material and the solid material under high pressure are updated by a specific equation of state.

Jones-Wilkins-Lee (JWL) equation of state [Zukas, Walters (1998)] is widely used for describing the expansion process of detonation products, in which the pressure is updated by

$$P = A(1 - \frac{\omega}{R_1 V})e^{-R_1 V} + B(1 - \frac{\omega}{R_2 V})e^{-R_2 V} + \frac{\omega E}{V} \tag{23}$$

where $E = \rho_0 e$ is the internal energy per initial volume, ω, A, B, R_1 and R_2 are user-defined constants.

The Mie-Grüneisen equation of state is capable of describing thermodynamics behavior for most metals under impact and explosion. The pressure in the porous material is related to that in the solid by [Johnson (1981)]

$$P(f,\rho,e) = (1-f)P_s(\rho_s, e_s) \tag{24}$$

where ρ and e are the density and specific internal energy of the porous material, respectively. ρ_s and e_s are the corresponding variables, given by

$$\rho_s = \frac{\rho}{(1-f)} \tag{25}$$

and

$$e_s = e \tag{26}$$

respectively. The third order approximate form of Mie-Grüneisen equation [Hallquist (1998)]

$$P_s = \rho_{s0}c_0^2(1 - \gamma_s\mu_s/2)P_H + \gamma_s\rho_s e_s \tag{27}$$

is implemented here for solid material, where

$$P_H = \mu_s + (2s-1)\mu_s^2 + (s-1)(3s-1)\mu_s^3 \tag{28}$$

and $\mu_s = \rho_s/\rho_{s0} - 1$ is the compression coefficient of the solid with ρ_{s0} being the solid density in the stress-free state. c_0, γ_0 and s are the constants of the solid.

The rate of the pressure is derived as

$$\dot{P} = -\dot{f}P_s + (1-f)\left(\frac{\partial P_s}{\partial \rho_s}\dot{\rho}_s + \frac{\partial P_s}{\partial e_s}\dot{e}_s\right) \tag{29}$$

The evolution of the porous density is expressed as

$$\dot{\rho} = -\rho D_m \tag{30}$$

where D_m is the (scalar) volumetric strain rate. Combining equations (16) , (25) and (30), the rate of the solid density can be calculated by

$$\dot{\rho}_s = -\rho_s\left(D_m - D_m^p - \frac{A_N\dot{\bar{\varepsilon}}^p}{1-f}\right) \tag{31}$$

The rate of the specific energy is given by

$$\dot{e}_s = \dot{e} = \frac{1}{\rho}\boldsymbol{\sigma} : \mathbf{D} = \frac{1}{\rho}(-PD_m + \mathbf{S} : \mathbf{D}_s) \tag{32}$$

where $\mathbf{D}_s$ is the deviatoric part of the total strain rate $\mathbf{D}$. Substituting equations. (16), (31) and (32) into equation (29), yields

$$\dot{P} = -BD_m + \alpha D_m^p + \beta A_N \dot{\bar{\varepsilon}}^p + \gamma_s \mathbf{S} : \mathbf{D}_s \tag{33}$$

where B is the equivalent bulk modulus of the porous material with the pressure updated by the EOS. B is related to the equivalent bulk modulus of the solid material B_s by $B = (1 - f)B_s$, and

$$B_s = \rho_s \frac{\partial P_s}{\partial \rho_s} + \gamma_s P_s \tag{34}$$

$$\alpha = B - (1 + \gamma_s)P \tag{35}$$

$$\beta = \frac{\partial p_s}{\partial \rho_s}\rho_s - P_s \tag{36}$$

Compared to the rate of pressure derived by Zuo et al. [Zou, Rice (2008)], the results presented here additionally account the effect of the nucleation of new voids.

3.3 Solution procedure

The stress update procedure of Gurson model has been depicted by Simonsen et al. [Simonsen, Li (2004)]. Here the Mie-Grüneisen equation is also coupled to the evolution process. The following two equations are solved with Newton iteration method.

$$f_1\left(D_m^p, D_{eq}^p\right) = D_m^p \frac{\partial \Phi}{\partial \sigma_{eq}} - D_{eq}^p \frac{\partial \Phi}{\partial \sigma_m} = 0 \tag{37}$$

$$f_2\left(D_m^p, D_{eq}^p\right) = \Phi\left(D_m^p, D_{eq}^p\right) = 0 \tag{38}$$

Given the stress $\boldsymbol{\sigma}^n$, plastic strain $\bar{\varepsilon}^{p,n}$ and void fraction f^n at time t_n, $\boldsymbol{\sigma}^{n+1}$, $\bar{\varepsilon}^{p,n+1}$ and f^{n+1} at time t_{n+1} can be updated as follows:

1. Elastic prediction

$$\mathbf{S}^t = \mathbf{S}^{Rn} + 2G^n \mathbf{D}_s^{n+1} \Delta t \tag{39}$$

$$\sigma_m^t = \sigma_m^n + B^n D_m^{n+1} \Delta t - \gamma_s \mathbf{S}^n : \mathbf{D}_s^{n+1} \tag{40}$$

2. Exam the yield function equation (13). If $\Phi \le 0$, let $\mathbf{S}^{n+1} = \mathbf{S}^t$ and $\sigma_m^{n+1} = \sigma_m^t$; else go to step 3.

3. Initialization ($Q_1 = \bar{\varepsilon}^p$, $Q_2 = f$). $k = 0$: $D_{m(0)}^p = 0$, $D_{\text{eq}(0)}^p = 0$, $Q_{1(0)}^{n+1} = \bar{\varepsilon}^{p,n}$, $Q_{2(0)}^{n+1} = f^n$, $\dot{Q}_{1(0)}^{n+1} = 0$, $\dot{Q}_{2(0)}^{n+1} = 0$. The following variables without special description are at the time t_{n+1}.

4. Calculate

$$
\begin{aligned}
\frac{\partial f_1}{\partial D_m^p} = &\frac{\partial \Phi}{\partial \sigma_{\text{eq}}} + D_m^p \left[\frac{\partial \sigma_m}{\partial D_m^p} \frac{\partial^2 \Phi}{\partial \sigma_{\text{eq}} \partial \sigma_m} + \sum_{i=1}^{2} \frac{\partial^2 \Phi}{\partial \sigma_{\text{eq}} \partial Q_i} \frac{\partial Q_i}{\partial D_m^p} \right] \\
& - D_{\text{eq}}^p \left[\frac{\partial \sigma_m}{\partial D_m^p} \frac{\partial^2 \Phi}{\partial \sigma_m^2} + \sum_{i=1}^{2} \frac{\partial^2 \Phi}{\partial \sigma_m \partial Q_i} \frac{\partial Q_i}{\partial D_m^p} \right]
\end{aligned}
\tag{41}
$$

$$
\begin{aligned}
\frac{\partial f_1}{\partial D_{\text{eq}}^p} = &D_m^p \left(\frac{\partial \sigma_{\text{eq}}}{\partial D_{\text{eq}}^p} \frac{\partial^2 \Phi}{\partial \sigma_{\text{eq}}^2} + \sum_{i=1}^{2} \frac{\partial^2 \Phi}{\partial \sigma_{\text{eq}} \partial Q_i} \frac{\partial Q_i}{\partial D_{\text{eq}}^p} \right) - \frac{\partial \Phi}{\partial \sigma_m} \\
& - D_{\text{eq}}^p \left(\frac{\partial \sigma_{\text{eq}}}{\partial D_{\text{eq}}^p} \frac{\partial^2 \Phi}{\partial \sigma_m \partial \sigma_{\text{eq}}} + \sum_{i=1}^{2} \frac{\partial^2 \Phi}{\partial \sigma_m \partial Q_i} \frac{\partial Q_i}{\partial D_{\text{eq}}^p} \right)
\end{aligned}
\tag{42}
$$

$$
\frac{\partial f_2}{\partial D_m^p} = \frac{\partial \sigma_m}{\partial D_m^p} \frac{\partial \Phi}{\partial \sigma_m} + \frac{\partial \sigma_{\text{eq}}}{\partial D_m^p} \frac{\partial \Phi}{\partial \sigma_{\text{eq}}} + \sum_{i=1}^{2} \frac{\partial \Phi}{\partial Q_i} \frac{\partial Q_i}{\partial D_m^p}
\tag{43}
$$

$$
\frac{\partial f_2}{\partial D_{\text{eq}}^p} = \frac{\partial \sigma_m}{\partial D_{\text{eq}}^p} \frac{\partial \Phi}{\partial \sigma_m} + \frac{\partial \sigma_{\text{eq}}}{\partial D_{\text{eq}}^p} \frac{\partial \Phi}{\partial \sigma_{\text{eq}}} + \sum_{i=1}^{2} \frac{\partial \Phi}{\partial Q_i} \frac{\partial Q_i}{\partial D_{\text{eq}}^p}
\tag{44}
$$

5. Calculate D_m^p and D_{eq}^p by

$$
\begin{bmatrix} \Delta D_{m(k)}^p \\ \Delta D_{\text{eq}(k)}^p \end{bmatrix} = \begin{bmatrix} \frac{\partial f_1}{\partial D_m^p} & \frac{\partial f_1}{\partial D_{\text{eq}}^p} \\ \frac{\partial f_2}{\partial D_m^p} & \frac{\partial f_2}{\partial D_{\text{eq}}^p} \end{bmatrix}^{-1} \begin{bmatrix} -f_1 \\ -f_2 \end{bmatrix}
\tag{45}
$$

$$
D_{m(k+1)}^p = D_{m(k)}^p + \Delta D_{m(k)}^p
\tag{46}
$$

$$
D_{\text{eq}(k+1)}^p = D_{\text{eq}(k)}^p + \Delta D_{\text{eq}(k)}^p
\tag{47}
$$

6. Update the equivalent stress σ_{eq} and the pressure P

$$
\sigma_{\text{eq}(k+1)} = \sigma_{\text{eq}}^t - 3G\Delta t D_{\text{eq}(k+1)}^p
\tag{48}
$$

$$
P_{k+1} = -\sigma_{m(k+1)} = -\sigma_m^t + \alpha \Delta t D_{m(k+1)}^p + \beta A_N \Delta t \dot{Q}_{1(k+1)}
\tag{49}
$$

7. Update $\dot{Q}_1$, $\dot{Q}_2$. Equations (49) and (50) are solved simultaneously.

$$\dot{Q}_{1(k+1)} = \frac{\sigma_{m(k+1)}D^p_{m(k+1)} + \sigma_{\text{eq}(k+1)}D^p_{\text{eq}(k+1)}}{(1-f)Y} \tag{50}$$

$$\dot{Q}_{2(k+1)} = (1-f)D^p_{m(k+1)} + A_N\dot{Q}_{1(k+1)} \tag{51}$$

8. Update the internal variables

$$Q_{1(k+1)} = Q^n_1 + \Delta t\dot{Q}_{1(k+1)} \tag{52}$$

$$Q_{2(k+1)} = Q^n_2 + \Delta t\dot{Q}_{2(k+1)} \tag{53}$$

9. Check $|f_1|$, $|f_2|$. If $|f_1| < $ tol1 and $|f_2| < $ tol2 where tol1 and tol2 are the given tolerance values. If not converged, let $k = k+1$ and go to step 4.

The following derivatives are specified:

$$\frac{\partial\sigma_m}{\partial D^p_m} = -\alpha\Delta t - \beta A_N\Delta t\frac{\sigma_m}{(1-f)Y} \tag{54}$$

$$\frac{\partial\sigma_m}{\partial D^p_{\text{eq}}} = -\beta A_N\Delta t\frac{\sigma_{\text{eq}}}{(1-f)Y} \tag{55}$$

$$\frac{\partial\sigma_{\text{eq}}}{\partial D^p_{\text{eq}}} = -3G\Delta t \tag{56}$$

$$\frac{\partial\sigma_{\text{eq}}}{\partial D^p_m} = 0 \tag{57}$$

Details of the other derivatives can be found in [Simonsen, Li (2004)]. The main difference between the procedure provided here and that in [Simonsen, Li (2004)] lies on our consideration of pressure updated by EOS.

The study is focused on the deformation of metals driven by explosive which could produce high value of $\left|\frac{\sigma_m}{Y}\right|$ leading convergence problems. In application, q_2 is modified when $\left|\frac{\sigma_m}{Y}\right|$ reaches a certain value to

$$q_{2,\text{new}} = \left|\frac{Y}{\sigma_m}\right| \tag{58}$$

4   Crack modeling

As mentioned in section 1, the dynamic cracking is modeled by contact method with failure models. The material points reaching the specific failure condition naturally generate the crack surface. The multiple velocity field above and below the crack surface is ensured by the contact between the the surface particles and unfailed particles. Compared to CRAMP [Nairn (2003); Guo, Nairn (2006)], the method proposed here eliminates the crack surface model. So our method can be much more efficient both in 2D and 3D. Additionally, the robustness of the method used here is still maintained even when the material undergoes extreme deformation. The schematic diagram of crack modeling is shown in Figure 2, where the failed particles are represented by filled circles, the arrows indicate the contact force, and the background grid lines are dashed lines.
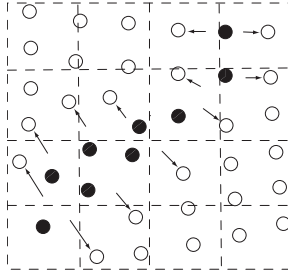

Figure 2: The schematic diagram of crack modeling

4.1   *Failure criteria*

Two kinds of failure criteria are used in this paper. When considering microscopic damage, the Gurson model is used with TEPLA-F failure condition, in which the initial void volume fraction of material points is randomly distributed. From a macroscopic view, the Gurson model reduces to J_2-flow theory when the microscopic void is neglected. In this situation, the macroscopic plastic deformation of the material at failure employs the Weibull random form. The random characterization of fragmentation is described by both the two approaches.

4.1.1   *TEPLA-F failure condition*

TEPLA-F failure condition was put forward based on the Gurson flow surface considering tensile plasticity and void growth [Johnson, Addessio (1988)]. The fracture conditions can be described in terms of the maximum allowable porosity f_f

and homogeneous plastic strain $\bar{\varepsilon}_p^f$ as

$$\left(\frac{f}{f_f}\right)^2 + \left(\frac{\bar{\varepsilon}_p}{\bar{\varepsilon}_p^f}\right)^2 = 1 \tag{59}$$

4.1.2 *Weibull statistical model for fracture*

The Weibull theory is normally used to analyze the failure of brittle material and fracture in ductile/brittle transition [Beremin (1983); Wang (1991); Lin, Shin (1996)], which was developed by Weibull [Weibull (1939)] in 1939 using the idea of the weakest link [Gumbel (1958)].

The Weibull theory for a uniaxial stress state can be written as [Jayatilaka (1979)]

$$P_f = 1 - \exp \int \left\{ -\left[\frac{\sigma - \sigma_{th}}{\sigma_0} \right]^m \right\} \frac{dA}{a} \tag{60}$$

where P_f is the probability of failure, A is the surface area and a is a unit area which is introduced for the consistency of units. σ_0, σ_{th}, m are respectively the mean strength, the threshold stress below which the material will not fail and a measure of scatter in the failure strengths of nominally identical components.

The equation (60) is the three-parameter Weibull theory. If $\sigma_{th} = 0$, the distribution becomes the two-parameter Weibull distribution as

$$P_f = 1 - \exp \int \left\{ -\left[\frac{\sigma}{\sigma_0} \right]^m \right\} \frac{dA}{a} \tag{61}$$

Typically, the two-parameter Weibull distribution is used, and it is employed in this paper.

For a uniform stress over the surface area, equation (61) can be rewritten using the known characteristic strength from the area a as

$$P_f = 1 - \exp\left\{ -(\sigma/\sigma_0)^m A/a \right\} \tag{62}$$

Fok et al. [Fok, Mitchell, Smart and Marsden (2001)] pointed out that the results for both two- and three-parameter predictions are similar when $A = 1000$. So the value $A = 1000$ will be used throughout the paper.

In this paper, the Weibull theory is employed on the basis of effective strain. That is to say , the ultimate effective strain is distributed randomly. When the strain arrives the critical level, the material will loose loading carrying capability. The Weibull statistical theory in terms of strain was also investigated by Tadashi [Tadashi (1969)] who proved that the failure behavior of brittle solid can also be explained in terms

of the stochastic process theory on the basis of strain. Therefore equation (62) takes the strain form as

$$P_{\mathrm{f}} = 1 - \exp\left\{-(\bar{\varepsilon}^p/\bar{\varepsilon}_0^p)^m A/a\right\} \tag{63}$$

4.2 Contact method

Because the single-valued mapping functions between background grid nodes and particles are used, a no-slip contact constraint is inherent in the standard MPM. However in problems involving impact and penetration, the inherent no-slip contact condition in the standard MPM may produce an artificial penetration resistance [Sulsky, Zhou, Schreyer (1995)]. Bardenhagen et al. [Bardenhagen, Brackbill, Sulsky (2000); Bardenhagen, Guilkey, Roessig, Brackbill, Witzel and Foster (2001)] proposed a contact/friction/separation algorithm in multi-velocity fields. Hu and Chen [Hu, Chen (2003)] presented a contact/sliding/separation algorithm in the multi-mesh environment to avoid interpenetration and allow separation in the gear contact process. Pan et al. [Pan, Xu, Zhang, Zhu, Ma and Zhang (2008)] proposed a three-dimensional multi-mesh contact algorithm for MPM, and Huang et al. [Huang, Zhang, Ma and Huang (2010)] developed a contact MPM algorithms for penetration simulation. In MPM3D, contact algorithm with USF, USL and MUSL formulation was implemented [Ma, Zhang, Huang (2010)], in which a local multi-mesh contact algorithm was developed to reduce computational cost, and an improved contact detection scheme was proposed.

The contact may occur when the momenta of two bodies are projected on to the same node. By comparing the nodal velocities $\mathbf{v}_i^1$ and $\mathbf{v}_i^2$, the contact between bodies I and II can be detected by [Pan, Xu, Zhang, Zhu, Ma and Zhang (2008)]

$$\left(\mathbf{v}_i^1 - \mathbf{v}_i^2\right) \cdot \mathbf{n}_i^1 > 0 \tag{64}$$

where $\mathbf{n}_i^1$ is the unit outward normal of body I at node i along the boundary.

As the momentum is required to be conserved, nodal momenta of contacting bodies need to be updated by [Pan, Xu, Zhang, Zhu, Ma and Zhang (2008)]

$$\bar{\mathbf{p}}_i^1 = \mathbf{p}_i^1 - \frac{m_i^2 \mathbf{p}_i^1 - m_i^1 \mathbf{p}_i^2}{m_i^1 + m_i^2} \cdot \mathbf{n}_i^1 \mathbf{n}_i^1 \tag{65}$$

$$\bar{\mathbf{p}}_i^2 = \mathbf{p}_i^2 + \frac{m_i^2 \mathbf{p}_i^1 - m_i^1 \mathbf{p}_i^2}{m_i^1 + m_i^2} \cdot \mathbf{n}_i^1 \mathbf{n}_i^1 \tag{66}$$

The acceleration along the normal of body I is equal to that of body II during the course of the contact, so that their nodal force must be updated by [Pan, Xu, Zhang, Zhu, Ma and Zhang (2008)]

$$\bar{\mathbf{f}}_i^1 = \mathbf{f}_i^1 - f_i^{\mathrm{nor}} \mathbf{n}_i^1 - f_i^{\mathrm{fric}} \mathbf{s}_i^1 \tag{67}$$

$$\bar{\mathbf{f}}_i^2 = \mathbf{f}_i^2 + f_i^{\text{nor}}\mathbf{n}_i^1 + f_i^{\text{fric}}\mathbf{s}_i^1 \tag{68}$$

where

$$f_i^{\text{nor}} = \frac{m_i^2 \mathbf{f}_i^{1,\text{int}} - m_i^1 \mathbf{f}_i^{2,\text{int}}}{m_i^1 + m_i^2} \cdot \mathbf{n}_i^1, \tag{69}$$

$$f_i^{\text{fric}} = \min\left(\mu f_i^{\text{nor}}, f_i^{\text{tan}}\right), \tag{70}$$

$$f_i^{\text{tan}} = \frac{\left(m_i^2 \mathbf{p}_i^1 - m_i^1 \mathbf{p}_i^2 + \left(m_i^2 \mathbf{f}_i^{1,\text{int}} - m_i^1 \mathbf{f}_i^{2,\text{int}}\right)\Delta t\right) \cdot \mathbf{s}_i^1}{\left(m_i^1 + m_i^2\right)\Delta t}, \tag{71}$$

and $\mathbf{s}_i^1$ is the unit tangential at node i along the boundary, μ is the coefficient of friction, Δt is the time step.

The unit surface normal vector is computed by the gradient of the nodal mass m_i^b in the individual body [Bardenhagen, Guilkey, Roessig, Brackbill, Witzel and Foster (2001)] as

$$\hat{\mathbf{n}}_i^b = \frac{1}{|\sum_p \nabla N_{ip} m_p^b|} \sum_p \nabla N_{ip} m_p^b \quad b = 1,2 \tag{72}$$

where m_p^b is the mass of particle p in body b. To guarantee the conservation of momentum in contact algorithms, the collinearity condition

$$\sum_{b=1}^{2} \mathbf{n}_i^b = 0 \tag{73}$$

must be satisfied at the contact surface. The following methods are implemented to make sure that the equation (73) is satisfied.

1. If body I is stiffer than body II, let $\mathbf{n}_i^1 = -\mathbf{n}_i^2 = \hat{\mathbf{n}}_i^1$ [Huang, Zhang, Ma and Huang (2010)].

2. If body I consists of failed particles and body II consists of unfailed ones, let $\mathbf{n}_i^1 = -\mathbf{n}_i^2 = \hat{\mathbf{n}}_i^2$.

The second method is proposed here to model dynamic cracking. The modified normal vector $\mathbf{n}_i^b$ insures the momentum conservation in the contact computation.

When a particle is failed, it loses its capacity to sustain load. The contact between the failed and unfailed bodies allows dual velocity field at background nodes, so that the crack will propagate along the failed particles.

5 Scaling behavior of fragmentation

Under rapidly applied loading such as an impact or a shock, materials may break into many pieces with propagation and interaction of many cracks. Despite of the complex process and apparent randomness of fragmentation, some remarkable scaling behavior features can be observed. A power-law distribution was observed by Oddershede et al. [Oddershede, Dimon, Bohr (1993)] in the breakup of brittle objects. The scaling exponent was found to be fairly sensitive to the shape of the object, but independent of the specific material, which can be interpreted as a self-organized critical phenomena [Inaoka, Toyosawa, Takayasu (1997)]. As in reference [Oddershede, Dimon, Bohr (1993)], the mass distribution of fragments $n(m)$ follows a power law, $n(m) \propto m^{-\beta}$. The measurements of the fracture distribution yield single event, so that it is more convenient to work with the cumulative distribution. The total number of fragments with masses larger than or equal to m is divided by m to make sure it exhibits with the same scaling exponent β as $n(m)$. Namely

$$N(m) = \frac{1}{m} \int_m^\infty n(m')\mathrm{d}m' \qquad (74)$$

In this paper, the metal shell driven by detonation is investigated. The fragments are constituted by the particles of the shell with the failed particles removed from it. In principle, a large number of pairwise calculations should be involved to generate good statistics of fragments. As to each particle i, all the other particles j must be looped over to calculate the pairwise distance d_{ij}. If d_{ij} is less than a prescribed cutoff distance d_{cut}, the pair of particles belong to the same fragment. Then an additional effort must be paid to find which pairs will constitute the whole fragment. Obviously, the particle based calculation is very expensive.

In the present paper, a background-grid-based technique is developed to calculate the statistics of fragments in material point method. Similar to the neighbor-list method [Rapaport (1996)] in molecular dynamics, a grid structure is set up by the method of linked list. Here the cells in the neighbor-list of a specific cell share at least one grid node with the specific cell. It is just necessary to loop over all the cells to get the statistics of fragments. The cell occupied by any fragment is defined as a fragmented cell. As shown in Figure 3, the fragmented cells are shaded. Starting from a specific fragmented cell, if its neighbor is also fragmented, the neighbors of the neighbor cell will be checked up. This process is carried out until there are no more neighbor cells are fragmented. The particles in this group of fragmented cells would belong to the same fragment. Ultimately the cells are divided into many groups each of which corresponds to a single piece of fragment. The process can be programmed in a recursive way to ensure simpleness and efficiency. In Figure

3, there are totally two groups of fragmented cells corresponding to two pieces of fragments which lie in the top left corner and bottom right corner respectively.
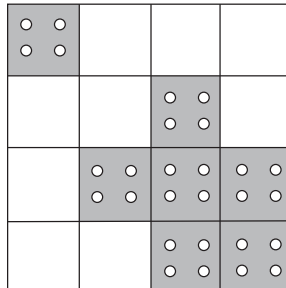

Figure 3: The cell structure

The statistical pseudo codes based on the background grid can be written as

```
nb_groups = 0;
for(int i=0;i<nb_cells;i++){
    Cell = cell_list[i];
    if (Cell belongs to any group)
        continue;
    if (Cell is fragmented)
    {
        Assign Cell to group_list[nb_groups];
        Check the neighbor cells of Cell;
    }
    nb_groups++;
}
```

where `nb_cells` is the total number of cells, `nb_groups` is the number of groups of the fragmented cells. The subfunction "Check the neighbor cells of Cell" can be written in a recursive way as

```
for(int i=0;i<nb_neighbors;i++){
    Cell_nei = neighbors_list[i];
    if (Cell_nei belongs to any group)
        continue;
    if (Cell_nei is fragmented)
    {
        Assign Cell_nei to group_list[nb_groups];
        Check the neighbor cells of Cell_nei;
    }
}
```

where `nb_neighbors` is the total number of neighbor cells of `Cell`.

The particle based method contains triple loops over the particles which would be very awkward as the number of particles increases. In contrast, it is only required to loop once over the cells in the background grid based method. In MPM, the number of particles is usually much larger than that of cells. Generally speaking, the interval of the cells is twice as that of particles. Apparently the background grid based method is much more efficient. Therefore there is no need to scan through the particles at all, which is different from the method [Rapaport (1996)] in molecular dynamics and making the approach here very efficient.

6 Numerical examples

6.1 Shear band analysis

In this section, a square specimen with length of $d = 10$ mm is studied. The top side of the square is stretched at a constant velocity of 0.1 mm/ms while the left and bottom sides are respectively constrained at horizontal and vertical direction. The results obtained from the MPM simulation are compared with those obtained by the explicit FEM solver of LS-DYNA to validate the Gurson model implemented here. A soft square spot with length of 1mm is located at the left bottom corner in the domain. The bilinear elastic-plastic constitutive relation is adopted to describe the plastic hardening of the matrix material. The constants of the matrix material and the Gurson model are listed in Tables 1 and 2, respectively. The initial porosity distribution in the soft spot is specified as 0.03 while it is set as 0.01 in the remaining domain. The pressure here is updated by Gurson model corresponding to equation (12).

Table 1: Material constants of the matrix material

ρ_s(g/mm^3)	E(MPa)	v	E_t(MPa)	σ_y(MPa)
0.0089	117000	0.35	500	150

Table 2: The constants of the Gurson model

q_1	q_2	f_c	f_f	f_N	ε_N	s_N
1.5	1	0.85	0.85	0.04	0.3	0.1

In the MPM simulation, the particle size is choosen as 0.05 mm while the background cell size is set as 0.1 mm. The element size in the FEM simulation equals to the background cell size used in the MPM simulation. Figure 4 compares the equivalent plastic strain distributions obtained by MPM and FEM along the diagonal line (from left upper corner to right down corner). Figure 5 compares the

void volume fraction distributions. It is shown that MPM and FEM give identical equivalent plastic strain and void volume fraction distributions at different times of 0.2 ms, 0.3 ms and 0.4 ms. The equivalent plastic strain nephograms obtained from MPM and FEM simulation are presented in Figure 6(a) and 6(b) respectively. Figure 7 depicts the mass normalized internal energy evolution of the soft spot and the remaining domain. The normalized internal energy of the soft spot grew more quickly than that of the remaining domain, which is resulted from the growth of the shear band along the diagonal line.

The shear band was initialized by the void growth and evolution. The example here validated the Gurson model implemented in our 3D explicit material point method code, MPM3D. The material just underwent small deformation in this section. Nevertheless under explosive loading, the material will suffer extreme large deformation in which case FEM will be evolved into the predicament of element distortion.
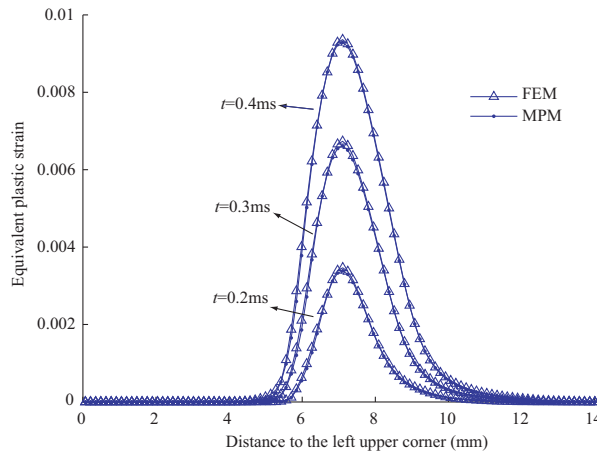
Figure 4: The equivalent plastic strain distributions along the diagonal line

6.2   *Fragmentation of a cylinder shell*

Tang et al. [Tang, Gu, Li, Hua and Sun (2003); Tang, Li, Sun, Sun, Jin and Gu (2006)] applied the high–speed photography to observe the expanding fracture of the 1045 steel cylinder shells driven by detonation. Here the model in [Tang, Gu, Li, Hua and Sun (2003)] is studied by MPM3D treating as a plain strain problem. The thickness of the steel shell is 4mm. Both the explosive and the steel shell are discretized by material points, generating 6284 and 12466 particles respectively. The mesh size is $0.5 \times 0.5 \times 0.5$mm. In this simulation, the explosive is RHT-901
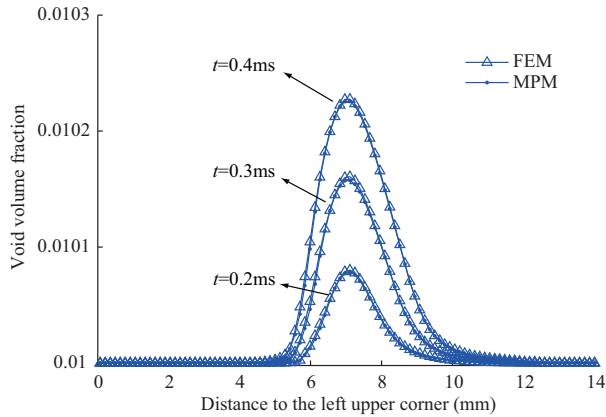
Figure 5: The void volume fraction distributions along the diagonal line
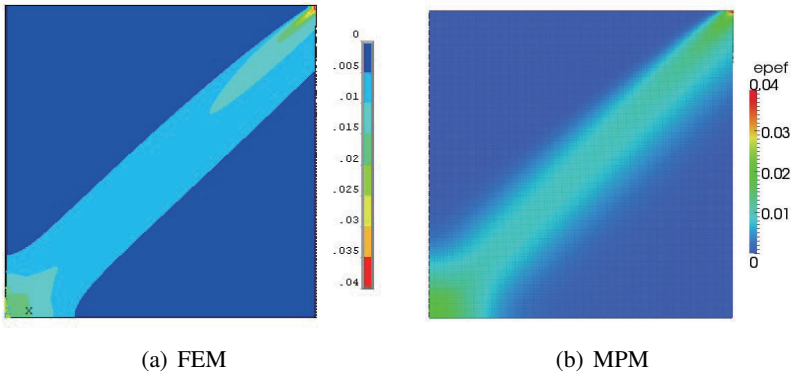

(a) FEM   (b) MPM

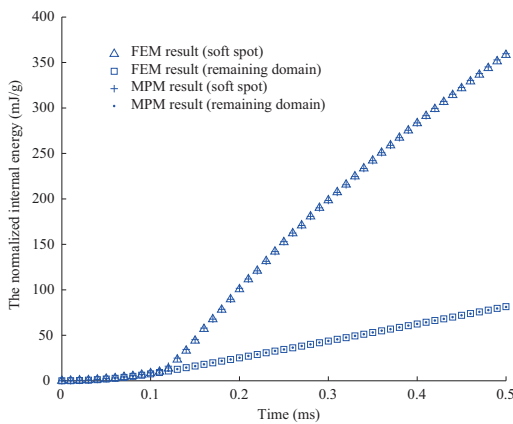Figure 6: The equivalent plastic strain distributions at 0.4 ms

Figure 7: The comparison of the normalized internal energy evolution obtained by FEM and MPM

just as that used in the experiment [Tang, Gu, Li, Hua and Sun (2003)]. RHT-901 has a density of 1.684kg/m³ and detonation velocity of 7790m/s. The parameters of JWL equation of state are taken from [Dong (1989)] as $A = 524.2$GPa, $B = 0.0321$GPa, $R_1 = 4.15$, $R_2 = 0.95$, $\omega = 0.3$. Here the simplified Johnson-Cook model

$$Y = (A + B(\bar{\varepsilon}^p)^N)(1 + C \ln \dot{\varepsilon}) \tag{75}$$

is used for the solid steel, where A, B, C, N are material constants. The constants of Johnson-Cook model for steel are listed in Table 3. The constants of Grüneisen EOS are $c_0 = 4.15$mm/μs, $s = 0.95$ and $\gamma_s = 0.3$.

Table 3: The constants of Johnson-Cook model [Chen, Chen, Xu, Chen and Huang (2007)]

E(MPa)	A(MPa)	B(MPa)	C	N	ρ_s(g/mm³)	ν
210000	507	320	0.064	0.28	0.0078	0.3

From the experiment [Tang, Gu, Li, Hua and Sun (2003)], the fracture strain ε_c of the shell is measured to be 0.43. So in the simulation, the mean value of the effective strain of the material at failure is set to 0.43 when the Weibull random failure scheme is employed. The two parameters of Weibull form are $\bar{\varepsilon}_0^p = 0.898$ and $m = 19.887$ respectively [Fok, Mitchell, Smart and Marsden (2001)]. On the other hand, TEPLA-F failure condition is incorporated into the Gurson flow model with $f_f = 0.2109$ [Lin, Fong (1995)] and $\bar{\varepsilon}_p^f = 0.43$. The constants of the Gurson model used here is listed in Table 4.

Table 4: The constants of Gurson model [Lin, Fong (1995)]

q_1	q_2	f_{0e}	f_{0s}	f_c	f_f	f_N	ε_N	s_N
1.5	1	0.005	0.0003	0.0021	0.2109	0.001	0.04	0.01

The simulation results of the fracture process with the Weibull random failure scheme and Gurson model are shown in Figure 8 and Figure 9, respectively. The time history of kinetic energy of the steel shell is plotted in Figure 10. Both the Gurson model and Weibull failure scheme give the similar prediction of the kinetic energy. At the beginning of detonation, the metal shell was accelerated with a high acceleration. After the steel shell fractured, the fragments were generated while the detonation product flows out through the gaps of fragments. Since then, the fragments with stable patterns went on moving forward at a relatively constant speed.

As shown in Figure 10, a box named "fracture box" is plotted where the curve slope decrease quickly to zero. The steel shell ruptured just in the "fracture box" resulting pieces of fragments. The fracture times, which are obtained in the numerical simulation as the time when there are no more fragments generated, are compared with the experiment in Table 5, and good agreements are observed.

Table 5: Fracture time of the shell

experiment	Weibull	Gurson
$15.4\mu s$	$15.0\mu s$	$15.5\mu s$

(a) $t = 10\mu s$ (b) $t = 20\mu s$ (c) $t = 30\mu s$ (d) $t = 40\mu s$
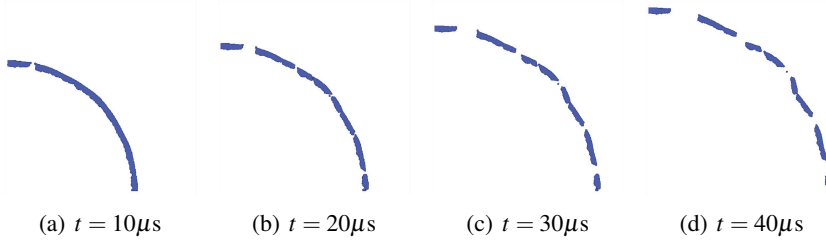
Figure 8: Fragmentation patterns obtained by the Weibull failure scheme

(a) $t = 10\mu s$ (b) $t = 20\mu s$ (c) $t = 30\mu s$ (d) $t = 40\mu s$
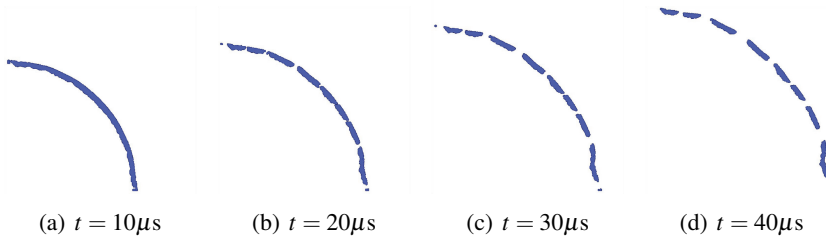
Figure 9: Fragmentation patterns obtained by the Gurson model

Reviewing the whole process of fracture, shear instability first occurred at the inner side of the shell where the material was compressed by detonation. The outer side of the shell soon got in tension along the circumferential direction, which may lead to tensile fracture. When the tensile fracture at the outer side met the shear instability band at the inner side, the mixed tensile-shear fracture grew up. The shear localization was risen by the high strain rate in detonation, resulting in the severe plastic deformation and necking of the shell. The mechanism is illustrated in Figure 11. In the simulation, the tensile-shear fracture can also be observed.
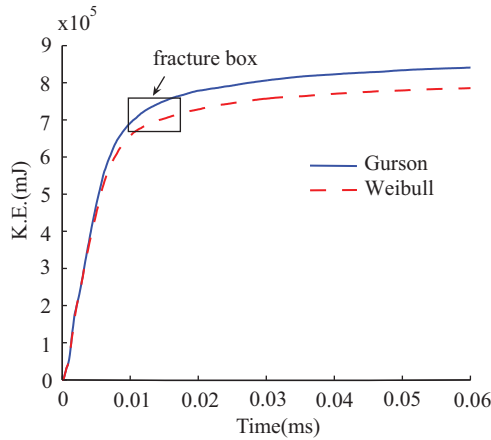
Figure 10: The evolution of kinetic energy of the shell

The material points located at the inner side of the shell failed firstly. When the expanding proceeded, the material points at the outer side lost their strength as the tensile stress increased. At last, cracks were initiated along the shear band. As in Figures 8 and 9, the necking appeared at the fracture area giving birth to the fragments with relatively smaller ends.
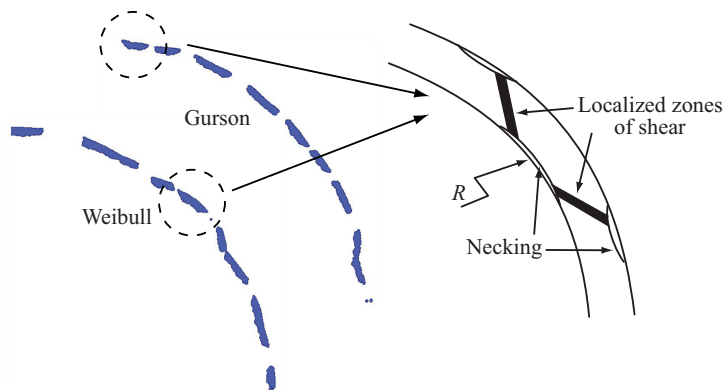

Figure 11: The shear localization and necking of the shell

Additionally, with the help of the Weibull failure scheme and the Gurson model with random initial particle voids, the fragments came out with different sizes and shapes in the simulation.

6.3   Fragmentation of a sphere shell

A toy problem is established by extending the problem in section 6.2 to a spherical one with a thickness of 4 mm and inner radius of 60 mm. Due to symmetry, a 1/8 model of the shell is studied with totally 1546509 particles. There are 636770 particles additionally used for the explosive. The interval of the background grid in each directions is 0.5 mm. The expansion of the shell is driven by detonation of explosive inside the shell just as that in the former case. The material constants of the explosive and metal shell are also the same as those used in section 6.2.

The resulting cracks and fragmentation patterns obtained from the Weibull failure scheme and the Gurson model are shown in Figures 12(a) and 12(b), respectively, where the failed particles are red while the unfailed particles are blue. The failed particles indicate the path of the cracks. Both the two approaches provide similar fragmentation patterns. However, the failed particles are almost at the whole outer surface when the Gurson model is used.

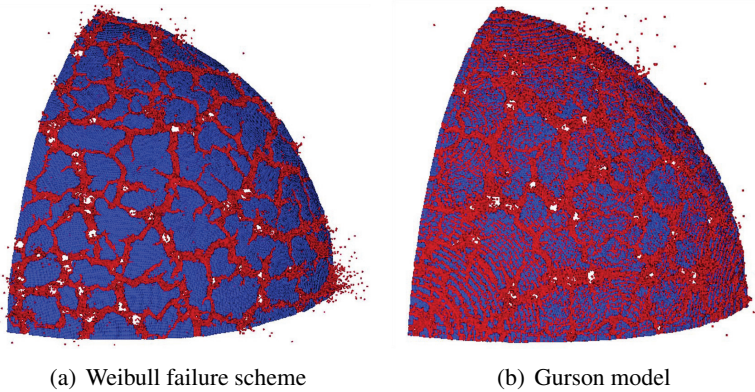

(a) Weibull failure scheme   (b) Gurson model

Figure 12: Cracks and fragmentation patterns

When the Gurson model was used, the void volume fraction of the particles at the inner side decreased under compression as shown in Figure 13(a). On the contrary, the voids at outer side expanded due to tension, thus the void grew, nucleated and coalesced, and eventually gave way to catastrophic cleavage fracture. Figure 13(b) provides the void volume fraction distribution of particles at outer side at $20\mu s$. Compared to the Weibull failure scheme, the Gurson model which considers the microscopic damage in the fracture better describes the ductile-brittle transition process. At the beginning of detonation, the strain rate was relatively low, and the ductile failure occurred. Then the strain rate reached a high level quickly. The flow strength increased with the increasing strain rate. Hence the stress level required

for cleavage could be reached before there was extensive plastic flow, and fractures took place in a brittle manner [Needleman, Tvergaard (2000)]. Reviewing Figure 10 in the cylinder case, the final kinetic energy of the shell is lower when using the Weibull form. The reason is probably that the shell tended to fracture in a more brittle way in the Weibull case, in which situation the shell broke up before sufficiently accelerated.

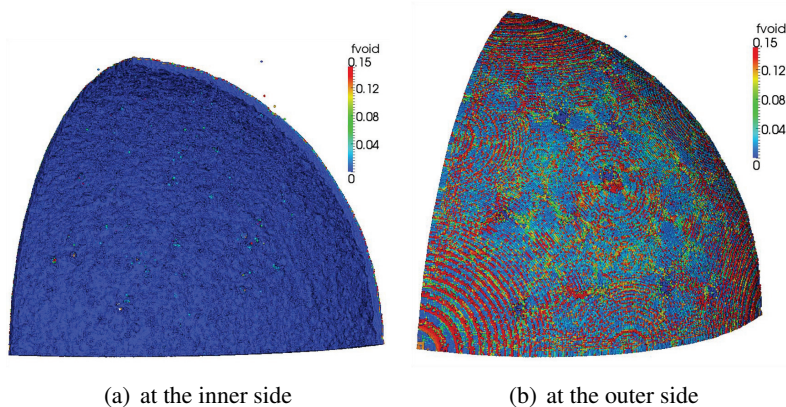(a) at the inner side   (b) at the outer side

Figure 13: The void volume fraction of the particles

The resulting statistical behavior of the fragments is obtained using the method proposed in section 5. As shown in Figure 14, both the Weibull failure scheme and the Gurson model predict that the distribution of fragments follows a power law with $\beta_w = 1.06$ and $\beta_g = 1.11$ respectively. Oddershede et al. [Oddershede, Dimon, Bohr (1993)] pointed out that the mass distribution of fragments essentially depends on the morphology of the fragmenting object rather than the specific material employed. They found that the power law exponent $\beta = 1.63$ for spherical balls, $\beta = 1.08$ for thin disks, and $\beta = 1.05$ for rods [Oddershede, Dimon, Bohr (1993)]. The sphere shell examined here is more structurally similar to a thin disk rather than a solid ball. Hence, the resulting β obtained in this paper is reasonable. It is found from Figure 14 that the distributions falls off more rapidly for masses above $m_0 = 0.5$g. The reason is that the scaling is presented for fragments of size smaller than the smallest dimension of the fragmenting object. In this example, the smallest dimension of the shell equals its thickness h(4mm), therefore, the characteristic cutoff mass $m_0 = \rho h^3 = 0.4992$g. Owing to the background-grid-based statistical technique, the time consumed for fragments statistics is negligible compared to the whole process of solution although the great number of particles are used in this example.
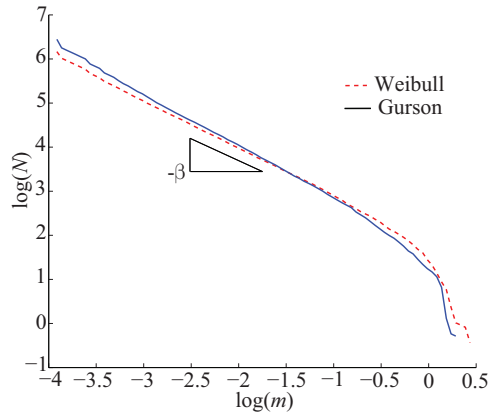
Figure 14: Logarithmic plot of the cumulative mass distribution of fragments

7   Conclusion

This paper presents a numerical model to analyze the metal fragmentation due to detonation. The Gurson model and Weibull failure scheme are implanted in the framework of MPM3D to achieve the goal. The crack is characterized by incorporating material failure process. Particles after failure are transformed to a different velocity field by contact method, which makes the crack surface not constrained by grid lines and free to propagate dynamically in any direction even when the material experiences large plastic strain increments.

Cylinder shell and sphere shell driven by detonation are simulated to validate the proposed method. The metal shell is accelerated due to the interaction with detonation production. Reasonable patterns of the fragmentation and fracture time of the shell are obtained from the simulations. Both the Weibull random scheme and Gurson model with randomly-distributed initial particle voids provide the random characterization of fragments. The advantage of using Gurson model is that the microstructure-based model gives a relatively realistic description of the ductile brittle transition. The statistical behavior of the fragments obtained from the solution follows a power law. The efficient method proposed to get the statistics of fragments further demonstrates that MPM is a powerful tool for studying the fragmentation phenomenon.

References

Arnold, W.; Rottenkolber, W. (2008): Fragment mass distribution of metal cased explosive charges. *International Journal of Impact Engineering*, vol.35, pp.1393–1398

Bardenhagen, S. G.; Brackbill, J. U.; Sulsky, D. (2000): The material point method for granular materials. *Computer Methods in Applied Mechanics and Engineering*, vol.187, pp.529–541

Bardenhagen, S. G.; Guilkey, J. E.; Roessig, K. M.; Brackbill, J. U.; Witzel, W. M.; Foster, J. C. (2001): An improved contact algorithm for the material point method and application to stress propagation in granular material. *CMES: Computer Modeling in Engineering and Science*, vol.2(4), pp.509–522

Beremin, F. M. (1983): A local criterion for cleavage fracture of a nuclear pressure vessel steel. *Metallurgical and Materials Transactions A*, vol.14A, pp.2277–2287

Brackbill, J. U.; Kothe, D. B.; Ruppel, H. M. (1988): Flip: a low dissipation, particle-in-cell method for fluid flow. *Computer Physics Communications*, vol.48, pp.25–38

Chu, C. C.; Needleman, A. (1980): Void nucleation effects in biaxially stretched sheets. *Journal of Engineering Materials and Technology*, vol.102, pp.249–256

Chen, G.; Chen, Z. F.; Xu, W. F.; Chen Y. M. Huang X. C. (2007): Investigation on the J-C ductile fracture parameters of 45 steel. *Explosion and Shock Waves*, vol.27(2), pp.131–135 [in Chinese]

Diehl, A.; Carmona, H. A.; Araripe, L. E.; Andrade, JS. Jr.; Farias, G. A. (2000): Scaling behavior in explosive fragmentation. *Physical Review E*, vol.62(4), pp.4742–4746

Dong, H. S. (1989): High energy explosive and some related properties. Sceience Press, Beijing. [in Chinese]

Fok, S. L.; Mitchell, B. C.; Smart, J.; Marsden, B. J. (2001): A numerical study on the application of weibull theory to brittle matrials. *Engineering Fracture Mechanics*, vol.68, pp.1171–1179

Goto, D. M.; Becker, R.; Orzechowski, T. J.; Springer, H. K.; Sunwoo, A. J.; Syn, C. K. (2008): Investigation of the fracture and fragmentation of explosively driven rings and cylinders. *International Journal of Impact Engineering*, vol.35, pp.1547–1556

Guilkey, J. E.; Harman, T. B.; Banerjee, B. (2007): An Eulerian-Lagrangian approach for simulating explosions of energetic devices. *Computers & Structures*, vol.85, pp.660–674

Gumbel, E. J. (1958): Statistical of Extremes. Columbia University Press, New York.

Guo, Y. J.; Nairn, J. A. (2006): Three-dimesional dynamic fracture analysis using the materail point mehtod. *CMES: Computer Modeling in Engineering and Science*, vol.16, pp.141–156

Gurran, D. R.; Seaman, L.; Shockey, D. A. (1987): Dynamic failure of solids. *Physics Reports*, vol.147, pp.253

Gurson, A. L. (1977): Continuum theory of ductile rupture by void nucleation and growth: Part 1. Yield criteria and flow rules for porous ductile media. *Journal of Engineering Materials and Technology*, vol.99, pp.2–15

Hallquist, J. O. (1998): LS-DYNA Theoretical Manual. Livermore Software Technology Corporation.

Hu, W.; Chen, Z. (2003): A multi-mesh MPM for simulating the meshing process of spur gears. *Computers & Structures*, vol.81, pp.1991–2002

Hu, W.; Chen, Z. (2006): Model-based simulation of the synergistic effects of blast and fragmentation on a concrete wall using the MPM. *International Journal of Impact Engineering*, vol.32, pp.2066–2096

Huang, P.; Zhang, X.; Ma, S.; Huang, X. (2010): Contact algorithms for the material point method in impact and penetration simulation. *International Journal for Numerical Methods in Engineering*, vol.85, pp.498–517

Inaoka, H.; Toyosawa, E.; Takayasu, H. (1997): Aspect Ratio Dependence of Impact Fragmentation. *Physical Review Letters*, vol.78, pp.3455

Jayatilaka, A. S. (1979): Fracture of Engineering Brittle Materials. Applied Sciece Publishers, London.

Johnson, J. N. (1981): Dynamic fracture and spallation in ductile solids. *Journal of Applied Physics*, vol.52, pp.2812

Johnson, J. N.; Addessio, F. L. (1988): Tensile plasticity and ductile fracture. *Journal of Applied Physics*, vol.64(12), pp.6699–6712

Johnson, G. R.; Stryk, R. A.; Beissel, S. R. (1996): SPH for high velocity impact computations. *Computer Methods in Applied Mechanics and Engineering*, vol.139, pp.347–373

Liu, G. R.; Liu, M. B. (2003): Smoothed particle hydrodynamics: a meshfree particle method. World Scientific, Singapore.

Lin, X.; Fong, S. C. (1995): Ductile crack growth-II. Void nucleation and geometry effects on macroscopic fracture behavior. *Journal of the Mechanics and Physics of Solids*, vol.43(12), pp.1953–1981

Lin, X.; Shin, C. F. (1996): Ductile crack growth-III. transition to cleavage frature incorporation stastics. *Journal of the Mechanics and Physics of Solids*, vol.44(4), pp.603–639

Ma, S.; Zhang, X.; Lian, Y. P.; Zhou, X. (2009): Simulation of high explosive explosion using adaptive material point method. *CMES: Computer Modeling in Engineering and Science*, vol.39, pp.101–123

Ma, S.; Zhang, X.; Qiu, X. M. (2009): Comparison study of MPM and SPH in modeling hypervelocity impact problems. *International Journal of Impact Engineering*, vol.36, pp.272–282

Ma, Z. T.; Zhang, X.; Huang, P. (2010): An object-oriented MPM framework for simulation of large deformation and contact of numerous grains. *CMES: Computer Modeling in Engineering and Science*, vol.1, pp.61–88

Meyers, M. A. (1994): Dynamics Behavior of Materials. John Wiley & Sons.

Nairn, J. A. (2003): Material point method calculations with explicit cracks. *CMES: Computer Modeling in Engineering and Science*, vol.4(6), pp.649–663

Needleman, A.; Tvergaard, V. (2000): Numerical modleing of the dutcile-brittle trainsition. *International Journal of Fracture*, vol.101, pp.73–97

Oddershede, L.; Dimon, P.; Bohr, J. (1993): Self-organized criticality in fragmenting. *Physical Review Letters*, vol.71, pp.3107

Pan, X. F.; Xu, A. G.; Zhang, G. C.; Zhu, J. S.; Ma, S.; Zhang, X. (2008): Three-dimensional multi-mesh material point method for solving collision problems. *Communications in Theoretical Physics*, vol.49, pp.1129–1138

Rapaport, D. C. (1996): The Art of Molecular Dynamics Simulation. Cambridge University Press.

Shen, L. M.; Chen, Z. (2005): A silent boundary scheme with the material point method for dynamic analyses. *CMES: Computer Modeling in Engineering and Science*, vol.7(3), pp.305–320

Simonsen, B. C.; Li, S. F. (2004): Mesh-free simulation of ductile fracutre. *International Journal for Numerical Methods in Engineering*, vol.60, pp.1425–1450

Sulsky, D.; Chen, Z.; Schreyer, H. L. (1994): A particle method for history-dependent materials. *Computer Methods in Applied Mechanics and Engineering*, vol.118, pp.179–196

Sulsky, D.; Zhou, S. J.; Schreyer, H. L. (1995): Application of a particle-in-cell method to solid mechanics. *Computer Physics Communications*, vol.87, pp.236–252

Tadashi, H. (1969): Theory of failure of concrete and similar brittle solid on the basis of strain. *International Journal of Fracture Mechanics*, vol.5(1), pp.73–79

Tang, T. G.; Gu, Y.; Li, Q. Z.; Hua, J. S.; Sun, X. L. (2003): Expanding fracture of steel cylinder shell by detonation driving. *Explosion and Shock Waves*, vol.23(6), pp.529–533 [in Chinese]

Tang, T. G.; Li, Q. Z.; Sun, X. L.; Sun, Z. F.; Jin, S.; Gu, Y. (2006): Strain-rate effects of expanding fracture of 45 steel cylinder shells driven by detonation. *Explosion and Shock Waves*, vol.26(2), pp.129–133 [in Chinese]

Tvergaard, V. (1981): Influence of voids on shear band instabilities under plane strain conditions. *International Journal of Fracture*, vol.17, pp.389–407

Tvergaard, V.; Needleman, A. (1984): Analysis of the cup-cone fracture in a round tensile bar. *Acta Metallurgica*, vol.32(1), pp.157–169

Wang, Y. Y. (1991): A two-parameter characterization of elastic-plastic crack-tip and applications to cleavage fracture. Ph.D. Thesis, Department of Mechanical Engineering, MIT.

Worswick, M. J.; Pick, R. J. (1990): Void growth and constitutive softening in a periodcally-voided solid. *Journal of the Mechanics and Physics of Solids*, vol.38, pp.601

Worswick, M. J.; Pick, R. J. (1995): Void growth and coalescence during high velocity impact. *Mechanics of Materials*, vol.19, pp.293–309

Weibull, W. (1939): A statistical theory of strength of materials. *Royal Swedish Institute for Engineering Research*, pp.1–45

Weibull, W. (1951): A statistical distribution function of wide applicability. *Journal of Applied Mechanics*, vol.18, pp.253

Zhang, H. W.; Wang, K. P; Chen Z. (2009): Material point method for dynamic analysis of saturated porous media under external contact/impact of solid bodies. *Computer Methods in Applied Mechanics and Engineering*, vol.198(17–20), pp.1456–1472

Zukas, J.; Walters, W. (1998): Explosive Effects and Applications. Spinger.

Zou, Q. H.; Rice, J. R. (2008): An implicit algorithm for a rate-dependent ductile failure model. *Journal of Applied Physics*, vol.104, pp.083526